impact into a thin brittle lithosphere overlying a fluid or a ductile layer that behaves as a fluid during crater collapse[10]. The apparent abruptness of Transition III on Europa (Figs 1, 2) is consistent with a sharp phase change at depth, such as an ice–liquid interface, but may also represent a rapid transition to the hot base of the ice shell where the ice is near melting and very ductile. It seems that the base of the icy shell is not much deeper, but the inferred Transition III depth at least indicates a minimum ice shell thickness of around 19–25 km. Europa's known impact craters are unlikely to excavate ocean material directly to the surface, however (unless the material is trapped in isolated shallow reservoirs). The largest crater, Tyre, excavates down to only about 3 km (~30–40% of the transient crater depth[18]), or around 15% of the minimum shell thickness.

Systematic mapping of impact crater shape and morphology provides a robust (and free) means of sampling icy satellite interiors. Ice rheology is dependent on temperature[22] and these transition diameters provide new constraints on the comparative thermal structure of these satellites. Transitions II and III are 2–4 times shallower on Europa than on Ganymede or Callisto, indicating that the rheologic structure of Europa's outer shell is similarly thinner than on Ganymede and Callisto. As heat flow scales roughly linearly with the thickness of the stagnant non-convecting lid[10] (possibly represented by Transition II), heat flow should to first order also be 2–4 times higher on Europa, depending on epoch. Transition III constrains Europa's ice shell to be at least 19–25 km thick, consistent with that required for convection to proceed within the ice shell[10] and favouring diapirism of the lower shell for the origin of ovoid features and chaos terrains (refs 7, 29 and P.S. and R. Pappalardo, manuscript in preparation). The minimum shell thickness strongly supports thick ice shell models in general, and associated interpretations of geologic features[2,7,29]; it may also indicate the depth to Europa's ocean, or at least the beginning of the hot basal layer of the floating ice shell. □

Methods

Crater depths have been measured from Galileo and Voyager data using three techniques: stereo digital elevation models (DEMs), photoclinometry DEMs, and shadow length measurements. Stereo DEMs resolve only the large craters Pwyll, Mannann'an, and Cilix (diameters 19–27 km) on Europa, and several anomalous dome craters on Ganymede. Photoclinometry in two horizontal dimensions can be used with single low-sun images to map topography from relative brightness. My photoclinometry technique includes the use of low-phase-angle images to model local albedo, thus reducing or eliminating one of the major systematic sources of error in photoclinometry. This technique is used here primarily to confirm the stereo and shadow measurements, but is the primary source of topographic data for the multiring basins Callanish and Tyre. Photoclinometry was also used to map topography across additional anomalous dome craters on Ganymede, supporting the conclusion that they have raised floors based on limited stereo data described above. I also use low-resolution controlled stereo DEMs to control the long-wavelength component of high-resolution photoclinometry DEMs. This was especially useful for Pwyll (Fig. 1). Height measurements based on triangulation of shadow lengths are used for all craters on Europa, Ganymede and Callisto smaller than ~15 km across. Depth measurement errors include systematic errors due to technique and those due to variations in topography along the rim crest. Systematic errors rarely exceed 10%. Variations in rim height approach about 100 m for large craters such as Pwyll. These data supercede the depth/diameter statistics for Ganymede and Callisto based on lower-resolution Voyager data[12,19]; no Voyager-based measurements were possible for craters on Europa.

Received 21 January; accepted 8 April 2002.

1. Greenberg, R. Tides and the biosphere of Europa. *Am. Sci.* **90,** 48–55 (2002).
2. Pappalardo, R. *et al.* Does Europa have a subsurface ocean? Evaluation of the geologic evidence. *J. Geophys. Res.* **104,** 24015–24056 (1999).
3. Kivelson, M. *et al.* Galileo magnetometer measurements: A stronger case for a subsurface ocean on Europa. *Science* **289,** 1340–1343 (2000).
4. Zimmer, C., Khurana, K. & Kivelson, M. Subsurface oceans on Europa and Callisto: Constraints from Galileo magnetometer observations. *Icarus* **147,** 329–347 (2000).
5. Greenberg, R., Geissler, P., Tufts, B. R. & Hoppa, G. Habitability of Europa's crust: The role of tidal-tectonic processes. *J. Geophys. Res.* **105,** 17551–17562 (2000).
6. Hoppa, G., Tufts, B. R., Greenberg, R. & Geissler, P. Formation of cycloidal features on Europa. *Science* **285,** 1899–1903 (1999).
7. Rathbun, J., Musser, G. & Squyres, S. Ice diapirs on Europa: Implications for liquid water. *Geophys. Res. Lett.* **25,** 4157–4160 (1998).
8. Kivelson, M., Khurana, K. & Volwerk, M. *Icarus* (in the press).
9. Kivelson, M. *et al.* Europa and Callisto: Induced or intrinsic fields in a periodically varying plasma environment. *J. Geophys. Res.* **104,** 4609–4625 (1999).
10. McKinnon, W. Convective instability in Europa's floating ice shell. *Geophys. Res. Lett.* **26,** 951–954 (1999).
11. Pike, R. in *Mercury* (eds Vilas, F., Chapman, C. & Matthews, M.) 165–273 (Univ. Arizona Press, Tucson, 1988).
12. Schenk, P. Ganymede and Callisto: Complex crater formation and planetary crusts. *J. Geophys. Res.* **96,** 15635–15664 (1991).
13. McKinnon, W. & Melosh, H. J. Evolution of planetary lithospheres: Evidence from multiring basins on Ganymede and Callisto. *Icarus* **44,** 454–471 (1998).
14. Moore, J. M. *et al.* Large impact features on Europa: Results from the Galileo nominal mission. *Icarus* **135,** 127–145 (1998).
15. Moore, J. M. *et al.* Large impact features on Europa: Results from the Galileo GEM mission. *Icarus* **151,** 93–111 (2001).
16. Turtle, E. & Pierazzo, E. Thickness of a Europan ice shell from impact crater simulations. *Science* **294,** 1326–1328 (2001).
17. Williams, K. & Zuber, M. Measurement and analysis of lunar basin depths from Clementine data. *Icarus* **131,** 107–122 (1998).
18. Melosh, H. J. *Impact Cratering* (Oxford Press, Oxford, 1989).
19. Schenk, P. Central pit and dome crater: Exposing the interiors of Ganymede and Callisto. *J. Geophys. Res.* **98,** 7475–7498 (1993).
20. Schenk, P. & Ridolfi, F. Morphology and scaling of ejecta deposits on icy satellites. *Geophys. Res. Lett.* (in the press).
21. Dombard, A. & McKinnon, W. Long-term retention of impact crater topography on Ganymede. *Geophys. Res. Lett.* **27,** 3663–3666 (2000).
22. Durham, W., Kirby, S. & Stern, L. Creep of water ices under planetary conditions: A compilation. *J. Geophys. Res.* **102,** 16293–16301 (1997).
23. Turtle, E. & Ivanov, B. Numerical simulations of crater excavation and collapse on Europa: Implications for ice thickness. *Lunar Planet. Sci. XXXIII* abstr. no. 1431 (2002).
24. Melosh, H. J. & Gaffney, E. Acoustic fluidization and the scale dependence of impact crater morphology. *J. Geophys. Res.* **88,** A830–A834 (1983).
25. McKinnon, W. & Schenk, P. Estimates of comet fragment masses from impact crater chains on Callisto and Ganymede. *Geophys. Res. Lett.* **22,** 1829–1832 (1995).
26. Anderson, J., Lau, E., Sjogren, W., Schubert, G. & Moore, W. Gravitational constraints on the internal structure of Ganymede. *Nature* **384,** 541–543 (1996).
27. Anderson, J. *et al.* Shape, mean radius, gravity field and internal structure of Callisto. *Icarus* **153,** 157–161 (2001).
28. Passey, Q. & Shoemaker, E. in *Satellites of Jupiter* (ed. Morrison, D.) 379–433 (Univ. Arizona Press, Tucson, 1982).
29. Collins, G., Head, J., Pappalardo, R. & Spaun, N. Evaluation of models for the formation of chaotic terrain on Europa. *J. Geophys. Res.* **105,** 1709–1716 (2000).

Acknowledgements

This work was supported by NASA Planetary Geology and Geophysics.

Competing interests statement

The author declares that he has no competing financial interests.

Correspondence and requests for materials should be addressed to the author (e-mail: schenk@lpi.usra.edu).

Megagauss sensors

A. Husmann*, J. B. Betts†, G. S. Boebinger†, A. Migliori†, T. F. Rosenbaum* & M.-L. Saboungi‡

** The James Franck Institute and Department of Physics, The University of Chicago, Chicago, Illinois 60637, USA*
† National High Magnetic Field Laboratory, Los Alamos National Laboratory, Los Alamos, New Mexico 87545, USA
‡ Argonne National Laboratory, Argonne, Illinois 60439 USA, and CRMD-CNRS, Orléans, Cedex 2, France

Magnetic fields change the way that electrons move through solids. The nature of these changes reveals information about the electronic structure of a material and, in auspicious circumstances, can be harnessed for applications. The silver chalcogenides, Ag_2Se and Ag_2Te, are non-magnetic materials, but their electrical resistance can be made very sensitive to magnetic field by adding small amounts—just 1 part in 10,000—of excess silver[1–4]. Here we show that the resistance of Ag_2Se displays a large, nearly linear increase with applied magnetic field without saturation to the highest fields available, 600,000 gauss, more than a million times the Earth's magnetic field. These characteristics of large (thousands of per cent) and near-linear response over a large

field range make the silver chalcogenides attractive as magnetic-field sensors, especially in physically tiny megagauss (10^6 G) pulsed magnets where large fields have been produced but accurate calibration has proved elusive. High-field studies at low temperatures reveal both oscillations in the magnetoresistance and a universal scaling form that point to a quantum origin[5,6] for this material's unprecedented behaviour.

The drive to obtain the highest possible magnetic fields cuts across disciplinary boundaries, but it has particular implications for materials science. A magnetic field couples both to the orbital and the spin states of electrons in condensed matter and, if sufficiently powerful, can lift degeneracies, break symmetries, induce phase transitions, and generate new collective states such as the fractional quantum Hall effect. At 10^6 G (100 T), the magnetic energy $g\mu_B H$ (where g is the g-factor, μ_B is the Bohr magneton, and H is the magnetic field strength) can dominate all others, even approaching the thermal energy $k_B T$ at room temperature for a bare magnetic g-factor of 2 (here k_B is Boltzmann's constant, and T is temperature). Direct-current magnets are incapable of such extreme performance, but non-destructive pulsed fields of 40–60 T are possible via capacitor discharge with pulse widths of 10^{-2}–10^{-1} s (extended up to seconds when generator-driven)[7], and 50–300 T has been achieved in microcoil or laser-driven geometries over 10^{-8}–10^{-6} s timescales[8,9]. Realizing the full scientific promise of the technology requires small, robust magnetic-field sensors with large dynamic range, rapid response times, and repeatable performance. A simple scaling with magnetic field strength and temperature is desirable both for primary calibration of the field and for the treatment of substantial spatial[10] and temporal field gradients.

Our 60-T pulsed magnet provided a 16-ms-long pulse that had an exceptionally smooth inductive decay, free from high-frequency components because of the 1-MJ capacitor drive (Fig. 1a). The dual direct digital synthesizer (designed at the National High Magnetic Field Laboratory) and digital lock-in amplifier (LGK Corp.) was specially constructed to extract cleanly phase-sensitive voltages with uncommon accuracy over the entire field range during each magnet 'shot' (Fig. 1b). We plot in Fig. 2 the magnetic-field dependence up to 55 T of both the diagonal and off-diagonal components of the resistivity of $Ag_{2+\delta}Se$ from room temperature down to pumped helium temperature. The current was applied normal to the magnetic field direction. The normalized change in the longitudinal resistivity, $(\rho_{xx}(H) - \rho_{xx}(H=0))/\rho_{xx}(H=0) = \Delta\rho_{xx}/\rho_0$ (Fig. 2a), increases fivefold by $H = 55$ T at $T = 290$ K and almost 25-fold at $T = 1.5$ K. It evolves from a slightly superlinear to a slightly sublinear field dependence below $T = 110$ K. At the lowest temperatures an oscillatory component of the magnetoresistance emerges, but at no temperature is there any indication that the response is

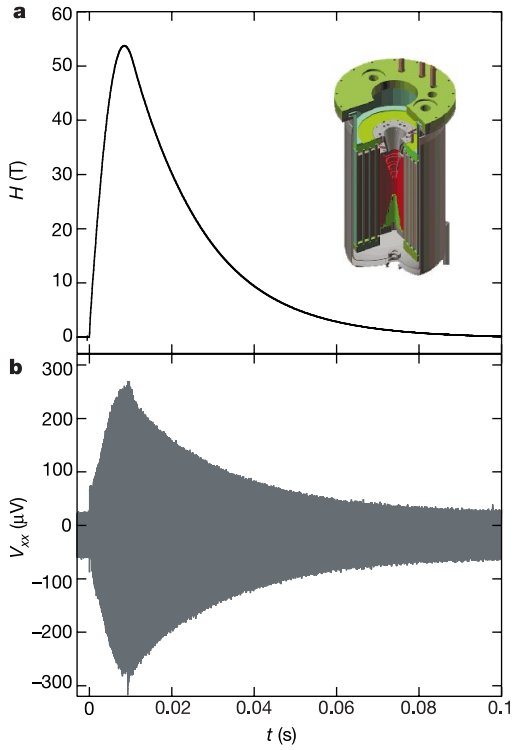

Figure 1 Pulsed magnet characteristics and low-noise data extraction. **a**, Capacitor-driven pulsed magnetic field profile as a function of time. Inset, diagram of the generator-driven 60-T long-pulse magnet, capable of providing up to 100 ms at peak field and a prime candidate for $Ag_{2+\delta}Se$ field sensors. It is about 2 m tall, 1 m in diameter, and features a 32-mm-diameter room-temperature bore. When energized it contains about 90 MJ of energy in the magnetic field. The windings of the electromagnet (shown red) are supported by cylindrical shells of high-strength, high-fracture-toughness steel. **b**, Data from a magnet 'shot'. A precision, low-distortion sine wave excitation drives a conventional 5-wire measurement of the longitudinal (V_{xx}) and Hall (V_{xy}) voltages at 156.3 kHz. A clock signal for a 16-bit analog-to-digital (A/D) converter is generated at an integer multiple of the excitation frequency. Raw data is obtained with nanosecond time jitter and megahertz raw Nyquist bandwidth. By setting the A/D clock at an integer multiple of the excitation, multiplying the A/D readings by software-generated sine and cosine functions, and averaging, a result similar to that from a commercial lock-in amplifier is produced, but with three key differences important for this experiment. First, we can adjust key measurement parameters after the magnet shot. We implement time-domain filtering of spikes, frequency-domain filtering of noise, adjust the phase, and adjust the averaging time constant after the shot and reversibly, tailoring the system response to the extreme pulsed magnet environment without having to retake data. Second, this method of synchronous digitization produces settling of the averaging 'filter' in exactly a half-cycle of excitation, thereby providing a response time that is much shorter than can be obtained with a conventional lock-in having an *RC* time constant final filter. This is essential for a low-noise measurement during a 16-ms experiment. Third, we can mathematically adjust the filter algorithm time centre such that there is no delay between a reported data point and the plotted magnetic field.

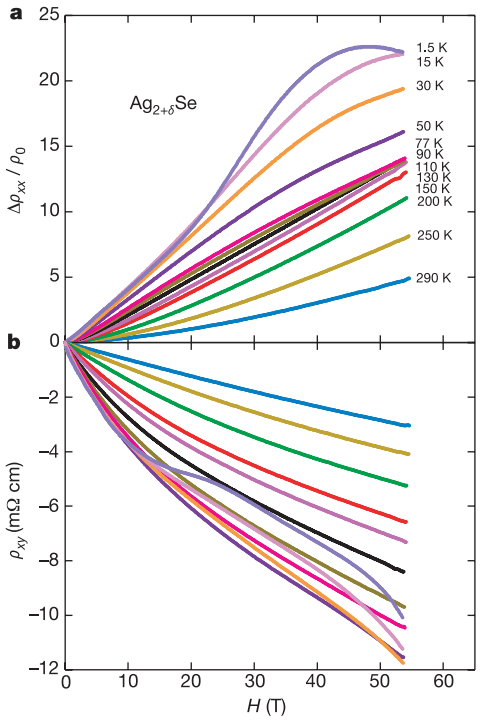

Figure 2 Magnetotransport of $Ag_{2+\delta}Se$ with $\delta \approx 10^{-4}$ in a 55-T pulsed magnetic field. **a**, The magnetoresistance normalized to its $H = 0$ value continues to climb over the full extent of the magnetic pulse at all temperatures T. **b**, Field variation of the Hall resistivity at the same temperatures (colour coded). In the low-T, low-H limit, electron density $n = 1.1 \times 10^{18}$ cm^{-3}.

saturating. Semiclassically, the orbital magnetoresistance is controlled by the product of the cyclotron frequency (ω_c) and the scattering time (τ), with a positive, quadratic magnetoresistance expected to saturate for $\omega_c\tau \approx 1$. In $Ag_{2+\delta}Se$, the quadratic behaviour required by symmetry considerations exists only below 0.01 T and the positive, approximately linear magnetoresistance continues to climb even for $\omega_c\tau > 50$, with no cut-off length scale in sight. The Hall resistivity, $\rho_{xy}(H)$ (Fig. 2b), demonstrates the expected n-type character for Ag-rich material. The crossover from intrinsic, small-gap semiconducting behaviour at high temperature (with a temperature-dependent carrier density gleaned from $d\rho_{xy}/dH|_{H\to 0}$) to a constant electron density $n = 1.1 \times 10^{18}$ cm^{-3} at low temperature occurs at $T_p \approx 80$ K.

After digital signal processing of the 156-kHz signal, the point-to-point noise in $\rho_{xx}(H)$ and $\rho_{xy}(H)$ is below 5 parts in 10,000, corresponding to a magnetic field uncertainty of less than 0.005 T at room temperature and ~0.001 T by 30 K over the entire field range. This markedly outperforms the present practice of determining H by integrating the voltage induced in a small pick-up coil inside the pulsed magnet. The small signal from such coils can be unreliable for H below a few tesla and, in a microcoil geometry, can introduce measurement uncertainties of ~12% at $H = 50$ T (ref. 8). Moreover, a magnetoresistive sensor provides an absolute calibration; there is no drift or accumulated error from integrating over time. Finally, in contrast to Hall bar sensors, these can be configured as two-lead devices that are intrinsically lower-power devices: $\rho_{xx}(H)$ measurements on a chip of silver selenide 0.4 × 0.4 × 1.0 mm dissipate less than 10 nW of power.

New techniques are being developed to exploit advances in high field capability, from refined medical imaging and high-field NMR spectroscopy for protein analysis, to picosecond measurements in a.c. fields and synchrotron X-ray scattering in pulsed, single-turn coils. Corresponding developments in magnet sensor technology are required. The state of the art for d.c. magnets is the Hall sensor, but at the cost of large power dissipation owing to high impedances. Large RC time constants (where R is resistance and C is capacitance) preclude any high-frequency applications. Pulsed magnets depend on pick-up coils, fine wire typically wound in 10–100-turn coils, sensitive to dH/dt. Calibration errors of 5–10% can be reduced by adding more turns n, but this increases the L/R time constant (as n^2/n). (Here L is inductance.) Furthermore, the highest-field magnets have the smallest bores; smaller-volume pick-up coils have more-limited accuracy. The silver chalcogenides are uniquely suited to both d.c. and a.c. fields. They offer the important freedom of measuring $\rho_{xx}(H,T)$ at any suitably high frequency, avoiding noisy frequencies in a given application (for example, frequencies used in the radio-frequency coil of an MRI (magnetic resonance imaging) magnet) and minimizing crosstalk. They can be shrunk in size without reducing total signal, and placed near or upon the sample as magnet bore sizes, and field homogeneity, decrease.

We now consider if it is possible to collapse the data of Fig. 1 onto a universal curve that describes the behaviour of the material at all fields and temperatures. In conventional metals, the electrical conductivity is described in terms of the Boltzmann equation, assuming semiclassical transport with a single scattering time τ. In this framework, the magnitude of the magnetic field only enters into the expression for the normalized change in resistivity $\Delta\rho_{xx}/\rho_0$ in the form of the product $H\tau$. As $\tau^{-1} \propto \rho_0$, $\Delta\rho_{xx}/\rho_0$ can be expressed solely as a function of H/ρ_0. This functional dependence is known as Kohler's rule[11], and it is obeyed in a great number of metals where ρ_0 is tuned by impurity density or by temperature[12]. Kohler's rule is also a powerful test of whether the semiclassical approach can describe magnetotransport in exotic materials like the organic conductors[13] and the copper oxide superconductors[14]. In semiconductors, the carrier density n may vary when ρ_0 is tuned by changing T; a modified Kohler plot then scales $\Delta\rho_{xx}/\rho_0$ with $H/n\rho_0$.

At the extreme fields of our experiment, the Hall resistivity ρ_{xy} of semiconducting $Ag_{2+\delta}Se$ is no longer strictly linear in H (Fig. 2b), and n becomes a function of H. In order to account for this added dependence, we proceed by scaling $\Delta\rho_{xx}/\rho_0$ with $|\rho_{xy}|/\rho_0$ for $1.5 < T < 290$ K. $\Delta\rho_{xx}$ and ρ_{xy} are taken at the same H which, like n, enters only implicitly. The scans at each temperature are straight lines that lie parallel to each other on a log–log plot (not shown), indicating that one power law can serve as the general Kohler-type function. The curves do not coincide, but are shifted by a multiplicative factor that depends on T. Collapse onto a universal curve over almost three decades in $\Delta\rho_{xx}/\rho_0$ is demonstrated in Fig. 3 using the scaling form: $b(T)\Delta\rho_{xx}/\rho_0 = f(\rho_{xy}/\rho_0)$. The plot covers the field range from 55 T down to 0.5 T, below which the limitations of the pick-up coil used to calibrate our pulsed magnets introduce offsets and scatter into the data. Data for $T < 30$ K oscillate about the universal curve and are not shown. Magnetoresistance and Hall data from a second, more heavily doped $Ag_{2+\delta}Se$ sample similarly collapse onto a universal curve consistent with the same power law

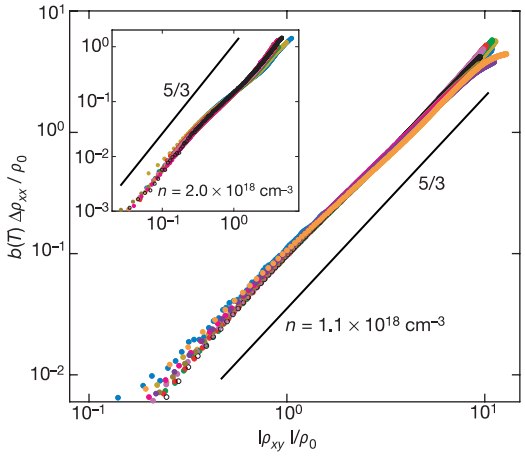

Figure 3 Scaling of the data of Fig. 2 using a modified Kohler plot where both $n(H)$ and H are implicit variables. The normalized magnetoresistivity ($\Delta P_{xx}/P_0$) scales with the normalized Hall resistivity ($|P_{xy}|P_0$) as a simple power law. The data collapse onto a universal curve for 0.5 T < H < 55 T and 30 K < T < 290 K when shifted by a multiplicative factor $b(T)$, where we have chosen $T = 290$ K as the baseline. The line follows $\Delta\rho_{xx} \propto \rho_{xy}^{5/3}$. Lower-temperature measurements exhibit quantum oscillations about the scaling curve and are not shown. Inset, collapse for a more highly doped sample of $Ag_{2+\delta}Se$ with carrier density n for $0.5 \le H \le 55$ T using the identical scaling form. Temperatures are 30, 50, 77, 87, 100, 150, 200, 250 and 290 K.

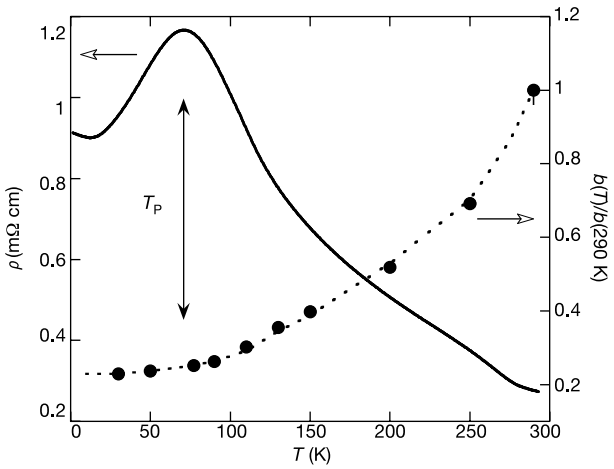

Figure 4 The scaling factor $b(T)$ and the longitudinal resistivity $\rho_{xx}(H = 0)$ as functions of temperature, suggesting different scaling character in the extrinsic and intrinsic semiconducting regimes (separated by the peak in ρ_{xx} at T_p).

(slope) and comparable absolute values for 30 K ≤ T ≤ 290 K and 0.5 T ≤ H ≤ 55 T (Fig. 3, inset). The quantum oscillations at low T are more pronounced at higher carrier density, and suggest that reducing n could extend the temperature range over which the monotonic power law scaling holds.

The 5/3 scaling power ($\Delta\rho_{xx} \propto \rho_{xy}^{1.65\pm0.1}$) reflects more than the nonlinear H-dependence of the Hall resistivity (Fig. 2). Scaling works in the low-field regime where $\rho_{xy} \propto H$ and in the high-field regime where $\rho_{xy}(H)$ departs from linearity; hand-in-hand variations of $\rho_{xx}(H,T)$ and $\rho_{xy}(H,T)$ naturally conspire to produce power-law scaling over the full range of field and temperature. Collapse onto one curve (Fig. 3), however, requires the sample-specific factor $b(T)$, whose general form is illustrated in Fig. 4. We index $b(T)$ to $\rho_{xx}(H = 0,T)$, noting the distinction between the constant carrier density regime below the resistance peak and the activated regime for $T > 80$ K (ref. 1). The fact that $b(T)$ becomes markedly less T-dependent below $T \approx 80$ K argues for a decomposition of $b(T)$ above and below T_p. At low T, ρ_{xx} increases with increasing T owing to phonon scattering, $b(T)$ is a nearly temperature-independent constant, and Kohler's rule serves as a reasonable construct for seeking universality. Complications ensue in the intrinsic semiconducting regime above T_p. We have nominally accounted for the variation of n with T and H by plotting $\Delta\rho_{xx}/\rho_0$ versus ρ_{xy}/ρ_0 rather than $H/n\rho_0$. Nonetheless, $b(T)$ rises steadily as $\rho_{xx}(T)$ falls, pointing to elements beyond semiclassical transport.

A quantum transport mechanism is certainly suggested by the pronounced oscillations in $\rho_{xx}(H)$ and $\rho_{xy}(H)$ that emerge at low T. They begin for $\rho_{xx} \approx 0.8$ mΩ cm, which corresponds to a sheet resistance (per unit cell layer) of 14 kΩ, close to the fundamental unit of resistance given by h/e^2 (where h is Planck's constant and e is the electronic charge). The oscillatory minima do not scale precisely as $1/H$, indicating a field-induced change in the electronic density of states beyond simple Landau level formation. Quantum fluctuations combined with disorder, caused for example by excess silver embedded in less-conducting material, can introduce length scales that are not set by the cyclotron radius, and can lead to a linear field dependence of the resistivity over decades in H (refs 5 and 6). (Classical approaches to inhomogeneous media[15] also can account for the unusual linear magnetoresistance in non-stoichiometric Ag_2Se and Ag_2Te, but are, at present, incompatible with experiments at small $\omega_c\tau$; refs 1, 4.)

The technological promise of the silver chacogenides lies precisely in the smooth and continued development of the magnetotransport characteristics over huge changes in applied field. Perhaps most telling, however, is the robust scaling relation that unfolds while relative energy scales change by orders of magnitude. The universal behaviour of Fig. 3 holds when the magnetic energy $g\mu_B H$ is small compared to all others, and when it rivals the gap energy[16], the thermal energy, and the energy scale set by the temperature dependence of the chemical potential. The 5/3 scaling exponent cannot be derived from classical transport equations, and may reflect a nonlinear coupling between different energy scales, common to hydrodynamic systems[17]. Whatever the underlying physical mechanism, the observed universal behaviour over decades in field and temperature permits predictive power for $Ag_{2+\delta}Se$ sensor response, with every expectation of magnetic field sensitivity well beyond 10^6 G. □

Methods

High-purity Ag_2Se was ground and loaded into outgassed fused silica ampoules inside a helium glove-box, and appropriate amounts of silver were added to reach the desired compositions. The samples were sealed under vacuum, heated in a rocking furnace above its melting point for 24 h, and left to cool in a horizontal position. Regularly shaped sensors of millimetre dimensions were cut on a diamond saw. Electrical leads could be attached easily with either silver epoxy or ultrasonically soldered InBi contacts. Rapid thermal cycling between liquid helium and room temperature can lead to initial changes of the resistance up to 5%, but sample characteristics stabilize after 5 to 7 quenches with no further changes. The variations appear to be dominated by shifts in the relative positions and quality of the electrical contacts. Lithographically defining micrometre-sized contact pads should improve reproducibility, and would permit the fabrication of submillimetre-sized sensors. Encapsulation in any thermally matched material (such as epoxy) for protection should not hinder performance.

Received 17 December 2001; accepted 2 April 2002.

1. Xu, R. *et al.* Large magnetoresistance in non-magnetic silver chalcogenides. *Nature* **390,** 57–60 (1997).
2. Chuprakov, I. S. & Dahmen, K. H. Large positive magnetoresistance in thin films of silver telluride. *Appl. Phys. Lett.* **72,** 2165–2167 (1998).
3. Ogorelec, Z., Hamzic, A. & Basletic, M. On the optimization of the large magnetoresistance of Ag_2Se. *Europhys. Lett.* **46,** 56–61 (1999).
4. Schnyders, H. S., Saboungi, M.-L. & Rosenbaum, T. F. Magnetoresistance in n- and p-type Ag_2Te: Mechanisms and applications. *Appl. Phys. Lett.* **76,** 1710–1712 (2000).
5. Abrikosov, A. Quantum magnetoresistance. *Phys. Rev. B* **58,** 2788–2794 (1998).
6. Abrikosov, A. Quantum linear magnetoresistance. *Europhys. Lett.* **49,** 789–793 (2000).
7. Boebinger, G. S., Lacerda, A. H., Schneider-Muntau, H. J. & Sullivan, N. The National High Magnetic Field Laboratory's pulsed magnetic field facility in Los Alamos. *Physica B* **294–295,** 512–518 (2001).
8. Mackay, K., Bonfim, M., Givord, D. & Fontaine, A. 50 T pulsed magnetic fields in microcoils. *J. Appl. Phys.* **87,** 1996–2002 (2000).
9. von Ortenberg, M. *et al.* The Humboldt high magnetic field center at Berlin. *Physica B* **294–295,** 568–573 (2001).
10. Drndic, M., Johnson, K. S., Thywissen, J. H., Prentiss, M. & Westervelt, R. M. Micro-electromagnets for atom manipulation. *Appl. Phys. Lett.* **72,** 2906–2908 (1998).
11. Kohler, M. Zur magnetischen Widerstandsänderung reiner Metalle. *Ann. Phys.* **32,** 211–218 (1938).
12. Pippard, A. P. *Magnetoresistance in Metals* (Cambridge Univ. Press, Cambridge, 1989).
13. McKenzie, R. H., Qualls, J. S., Han, S. Y. & Brooks, J. S. Violation of Kohler's rule by the magnetoresistance of a quasi-two-dimensional organic metal. *Phys. Rev. B* **57,** 11854–11857 (1998).
14. Harris, J. M. *et al.* Violation of Kohler's rule in the normal state magnetoresistance of $YBa_2Cu_3O_{7-\delta}$ and $La_{2-x}Sr_xCuO_4$. *Phys. Rev. Lett.* **75,** 1391–1394 (1995).
15. Herring, C. Effect of random inhomogeneities on electrical and galvanomagnetic measurements. *J. Appl. Phys.* **31,** 1939–1953 (1960).
16. Aliev, S. A. & Aliev, F. F. Band parameters and energy structure of β-Ag_2Se. *Izv. Akad. Nauk SSSR Neorg. Mater.* **21,** 1869–1872 (1985).
17. Tritton, D. J. *Physical Fluid Dynamics* (Van Nostrand Reinhold, New York, 1977).

Acknowledgements

We thank H. Hwang, L. P. Kadanoff and H. S. Schnyders for discussions, and the late R. Xu for technical assistance. The work at the University of Chicago and at Argonne National Laboratory was supported by DOE Basic Energy Sciences.

Competing interests statement

The authors declare that they have no competing financial interests.

Correspondence and requests for materials should be addressed to T.F.R. (e-mail: t-rosenbaum@uchicago.edu).

Rapidly recovering hydrogel scaffolds from self-assembling diblock copolypeptide amphiphiles

Andrew P. Nowak*†, Victor Breedveld†‡, Lisa Pakstis§, Bulent Ozbas§, David J. Pine†‡, Darrin Pochan§ & Timothy J. Deming*†

* *Departments of Materials and Chemistry;* † *Materials Research Laboratory;* ‡ *Department of Chemical Engineering, University of California, Santa Barbara, California 93106, USA*

§ *Department of Materials Science and Engineering and Delaware Biotechnology Institute, University of Delaware, Newark, Delaware 19716, USA*

Protein-based hydrogels are used for many applications, ranging from food and cosmetic thickeners to support matrices for drug delivery and tissue replacement[1–3]. These materials are usually prepared using proteins extracted from natural sources, which can give rise to inconsistent properties unsuitable for medical applications[4]. Recent developments have utilized recombinant DNA methods to prepare artificial protein hydrogels with specific association mechanisms and responsiveness to various stimuli[5,6]. Here we synthesize diblock copolypeptide amphiphiles containing charged and hydrophobic segments. Dilute solutions of these